

# Loopy-SLAM: Dense Neural SLAM with Loop Closures

Lorenzo Liso<sup>1\*</sup> Erik Sandström<sup>1\*</sup> Vladimir Yugay<sup>3</sup> Luc Van Gool<sup>1,2,4</sup> Martin R. Oswald<sup>1,3</sup>  
<sup>1</sup>ETH Zürich <sup>2</sup>KU Leuven <sup>3</sup>University of Amsterdam <sup>4</sup>INSAIT

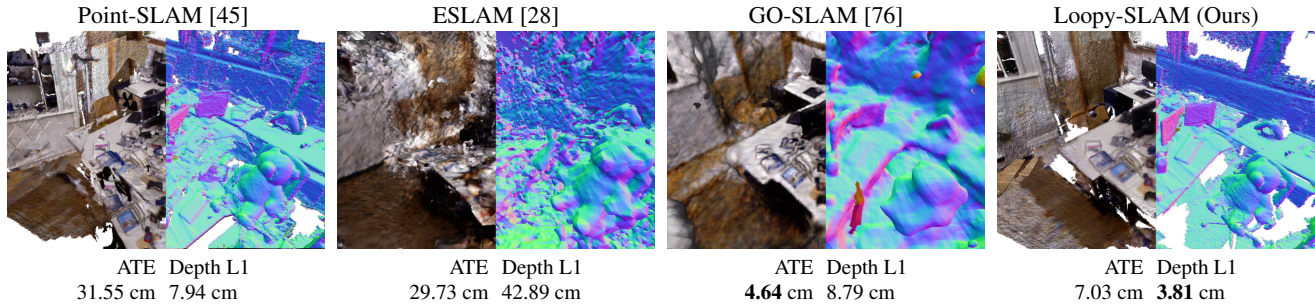


Figure 1. **Benefits of Loopy-SLAM.** While Point-SLAM yields high-fidelity reconstructions it does not implement loop closure and may duplicate geometries due to drift. ESLAM is faced by the same problem due to the lack of loop closure. GO-SLAM implements loop closure, but computes rather low quality map geometry. In contrast to GO-SLAM which requires to save the entire history of input frames used for mapping to update the map after loop closures, our approach anchors the neural scene representation on points which can simply be shifted without recomputing the dense map from scratch. We show the ATE RMSE and the depth L1 re-rendering error on the mesh for the TUM-RGBD `fr1_room` scene.

## Abstract

Neural RGBD SLAM techniques have shown promise in dense Simultaneous Localization And Mapping (SLAM), yet face challenges such as error accumulation during camera tracking resulting in distorted maps. In response, we introduce Loopy-SLAM that globally optimizes poses and the dense 3D model. We use frame-to-model tracking using a data-driven point-based submap generation method and trigger loop closures online by performing global place recognition. Robust pose graph optimization is used to rigidly align the local submaps. As our representation is point based, map corrections can be performed efficiently without the need to store the entire history of input frames used for mapping as typically required by methods employing a grid based mapping structure. Evaluation on the synthetic Replica and real-world TUM-RGBD and ScanNet datasets demonstrate competitive or superior performance in tracking, mapping, and rendering accuracy when compared to existing dense neural RGBD SLAM methods. Project page: [notchla.github.io/Loopy-SLAM/](https://notchla.github.io/Loopy-SLAM/).

## 1. Introduction

Online dense 3D reconstruction of scenes with an RGBD camera has been an active area of research for years [13, 36, 37, 48, 71, 77], and remains an open problem. Recently, several works proposed to optimize an encoder-free neural scene representation at test time [28, 45, 54, 61, 73, 77] with the potential to improve compression, extrapolate unseen geometry, provide a more seamless stepping point towards higher level reasoning such as 3D semantic prediction and leverage strong learnable priors as well as adapt to test time constraints via online optimization. One can make the distinction between *coupled* [28, 45, 46, 54, 57, 61, 73, 77] and *decoupled* [10, 31, 41, 76] solutions where *coupled* methods use the same representation for tracking and mapping while *decoupled* methods use independent frameworks for each task. Currently, the *decoupled* methods have achieved better tracking accuracy, but the decoupling creates undesirable data redundancy and independence since the tracking is performed independently of the estimated dense map. Tracking and mapping are coupled tasks and we therefore believe they should ultimately make use of the same scene representation. On the one hand, of the *coupled* methods, all but the concurrent MIPS-Fusion [57] implement just frame-to-model tracking, leading to significant camera drift on noisy real-world data, with corrupted maps as a result. On the other hand, the *decoupled* methods all make use of

\*Equal contribution.

multi-resolution hash grids [10, 31, 41, 76] and are therefore not easily transformable for map corrections *e.g.* as a result of loop closure, requiring expensive gradient-based updates and storing the input frames used for mapping for this purpose. Point-SLAM [45] has recently shown that a neural point cloud-based representation can be used as an efficient and accurate scene representation for mapping and tracking, but struggles to robustly track on noisy real-world data. Point-based representations are especially suitable for performing map corrections *e.g.* as a result of loop closure as they can be transformed fast and independently of each other. To this end, we introduce Loopy-SLAM, which inherits the data-adaptive scene encoding of Point-SLAM [45] and extends it with loop closure to achieve globally consistent maps and accurate trajectory estimation. Our **contributions** include:

- We propose Loopy-SLAM, a dense RGBD SLAM approach which anchors neural features in point cloud submaps that grow iteratively in a data-driven manner during scene exploration. We dynamically create submaps depending on the camera motion and progressively build a pose graph between the submap keyframes. Global place recognition is used to detect loop closures online and to globally align the trajectory and the submaps with simple and efficient rigid corrections directly on the scene representation. See Fig. 1.
- We propose a direct way of implementing loop closure for dense neural SLAM that does not require any gradient updates of the scene representation or reintegration strategies, contrary to previous works
- Traditionally, rigid submap registration may create visible seams in the overlapping regions. Our approach based on neural point clouds avoids this and we apply feature refinement of color and geometry at the end of the trajectory capture. We further introduce a feature fusion strategy of the submaps in the overlapping regions to avoid excessive memory usage and to improve the rendering performance.

## 2. Related Work

**Dense Visual SLAM and Online Mapping.** The seminal work of TSDF Fusion [11] was the starting point for a large body of works using truncated signed distance functions (TSDF) to encode scene geometry. KinectFusion [36] was among the first to show that dense mapping and tracking using depth maps can be achieved in real-time. A selection of works improved the scalability via voxel hashing [22, 37, 39] and octrees [14, 20, 49, 59] and pose robustness via sparse image features [6] and loop closure [7, 13, 30, 48, 71, 74]. Learning-based methods have also successfully been applied to the dense mapping problem, via learned updates of TSDF values [66] or neural fea-

tures [2, 21, 40, 62, 67]. A number of recent works do not need depth input and accomplish dense online reconstruction from RGB cameras only [5, 8, 25, 35, 47, 50, 55], but typically require camera poses as input. Lately, methods relying on test-time optimization have become popular again due to the wide adaptability of differentiable renderers for effective reprojection error minimization. For example, Neural Radiance Fields [32] inspired works for dense surface reconstruction [38, 63] and pose estimation [3, 26, 41, 65] and have matured into full dense SLAM pipelines [28, 45, 46, 54, 57, 61, 73, 77, 78], which use the same *coupled* scene representation for mapping and tracking. A selection of similar works choose to *decouple* mapping and tracking into independent pipelines to realize SLAM [10, 31, 41, 76]. Though the *decoupled* approach seems to currently achieve better tracking (since the representations can be optimized individually for each task), mapping and tracking are inherently *coupled* and we therefore believe they should be treated as such. We base our work on the recent Point-SLAM [45] framework which is especially suited for loop closure as the scene representation, consisting of points, is simple to transform. More importantly, map corrections can be achieved without a reintegration strategy per frame as in [13, 30, 76] which requires storing the *entire history* of input frames used for mapping and is resource-demanding for larger scenes.

**Loop Closure on Dense Maps.** The majority of dense methods tackling the problem of loop closure to attain a globally consistent dense map is done by subdividing the map into pieces, oftentimes called submaps [1, 4, 7, 9, 13, 16, 18, 22, 23, 29–31, 52, 57]. The submaps usually consist of a limited number of frames which are accumulated into a map. The submaps are then rigidly registered together via approximate global bundle adjustment via pose graph optimization [1, 7, 9, 14, 15, 17, 18, 23, 24, 30, 31, 48, 52, 57, 60, 72], sometimes followed by global bundle adjustment for refinement [7, 13, 48, 58, 72, 74]. Few works deviate from this methodology by optimizing a deformation graph [68, 70, 71]. Specifically, ElasticFusion [71] optimizes a sparse as-rigid-as-possible deformation graph to register a temporally recent *active* submap against an *inactive* global submap. Since the *active* map is deformed into the *inactive* map, drift cannot be well tackled in the *inactive* map, which can lead to global map inconsistencies. We therefore also split our map into submaps and apply online pose graph optimization. Among the recent dense neural SLAM works, some apply loop closure [10, 31, 57, 76]. Orbeez-SLAM [10] and NEWTON [31] use a *decoupled* approach by employing ORB-SLAM2 [34] as the tracking system. Orbeez-SLAM and NEWTON use multi-resolution hash grids, requiring undesirable training iterations to perform map corrections. NEWTON uses multiple local spherical hash grids akin to submaps, but they focus mostly on

view synthesis. GO-SLAM [76] also uses a *decoupled* approach by extending DROID-SLAM [58] to the online loop closure setting and coupling it with a map via Instant-NGP [33]. Their results are impressive for tracking, but focus less on reconstruction and rendering. Furthermore, they also require training iterations to the hash grids to perform map corrections. Common for all works employing hash grids is that they require to store the entire history of input frames used for mapping to perform the map corrections. This limits their scalability. In contrast, by rigidly aligning submaps, our method is not restricted to the same degree. Concurrent to our work, MIPS-Fusion [57] is the only other work using a *coupled* approach with loop closure. They use MLPs which encode TSDFs to represent local submaps and perform loop closure by rigid registration of the submaps, but focus mainly on tracking and not on reconstruction nor rendering. Finally, MIPS-Fusion detects loop closures via co-visibility thresholds, which does not allow for the correction of large drifts, in contrast to global place recognition *e.g.* via [43], which we use.

### 3. Method

This section details our dense RGBD SLAM system. Specifically, we grow submaps of neural point clouds in a progressive manner as the scene space is explored. Frame-to-model tracking alongside mapping is applied on every *active* submap with a direct loss formulation (Sec. 3.1). Based on the camera motion, we dynamically trigger new *global* keyframes and associated submaps. When a submap is completed, we perform global place recognition to detect potential loop closures and add the relevant edges to a pose graph which is optimized using dense surface registration constraints. To further refine the scene representation, at the end of trajectory capture, we first apply feature fusion where the submaps overlap followed by color and geometry feature refinement (Sec. 3.2). Fig. 2 shows an overview.

#### 3.1. Neural Point Cloud-based SLAM

Point cloud-based SLAM as proposed in [45] lends itself for deforming a dense scene representation upon loop closures since both geometry and appearance are locally encoded in features anchored in a point cloud. These anchor points can be continuously shifted to deform the scene without the need to compute the dense representation from scratch using the original input data. To adapt the feature point cloud representation for loop closure updates, we redefine it as a set of  $s \in \mathbb{N}$  submaps, each containing a neural point cloud  $P^s$  with a collection of  $N$  neural points

$$P^s = \{(p_i^s, f_i^{s,g}, f_i^{s,c}) \mid i = 1, \dots, N^s\}, \quad (1)$$

each with a position  $p_i^s \in \mathbb{R}^3$  and with a geometric and color feature descriptor  $f_i^{s,g} \in \mathbb{R}^{32}$  and  $f_i^{s,c} \in \mathbb{R}^{32}$  respectively.

**Building Submaps Progressively.** Mapping and tracking are always performed on the *active* submap, defined as the most recently created submap. We associate the first frame of the submap as a *global* keyframe. The keyframe defines the pose of the submap in the global reference frame. We adopt the point adding strategy and dynamic resolution from Point-SLAM [45] and progressively grow each submap in a data dependent way to ensure efficiency and accuracy. Depth and color rendering follows [45] *i.e.* given a camera pose with origin  $\mathbf{O}$ , we sample a set of points  $x_i$  as

$$x_i = \mathbf{O} + z_i \mathbf{d}, \quad i \in \{1, \dots, M\}, \quad (2)$$

where  $z_i \in \mathbb{R}$  is the point depth and  $\mathbf{d} \in \mathbb{R}^3$  the ray direction. After the points  $x_i$  have been sampled, the occupancies  $o_i$  and colors  $\mathbf{c}_i$  are decoded using MLPs as

$$o_i = h(x_i, P^{s,g}(x_i)) \quad \mathbf{c}_i = g_\xi(x_i, P^{s,c}(x_i)). \quad (3)$$

Here,  $P^{s,g}(x_i)$  and  $P^{s,c}(x_i)$  denote the interpolated geometric and color features from the submap  $P^s$ . The geometry and color decoder MLPs are denoted  $h$  and  $g$ . We make a small adjustment to the mapping strategy. Apart from the feature, the decoders take the 3D point  $x_i$  as input, to which a learnable Gaussian positional encoding [56] is applied. However, while keeping the geometric MLP fixed, we allow the encoding to be optimized on the fly. At loop closure, when the points are shifted, they may not decode to the exact same value as before in their new location. Using an on-the-fly adaptive positional encoding gives the system a simple way of adjusting instead of updating the feature at each point, which is more expensive. For details on feature interpolation and rendering equations for color  $\hat{I}$  and depth  $\hat{D}$ , we refer to [45].

**Tracking and Mapping Losses.** Tracking and mapping are applied in an alternating fashion on the *active* submap and performed equivalently to [45]. For tracking we render  $M_t$  pixels across the RGBD frame and minimize the re-rendering loss to the sensor reading  $D$  and  $I$  as

$$\mathcal{L}_{\text{track}} = \sum_{k=1}^{M_t} \frac{|D_k - \hat{D}_k|_1}{\sqrt{\hat{S}_D}} + \lambda_t |I_k - \hat{I}_k|_1. \quad (4)$$

$\hat{D}$  and  $\hat{I}$  are the rendered depth and color,  $\hat{S}_D$  is the variance of  $\hat{D}$  (see [45]) and  $\lambda_t$  is a hyperparameter. For mapping we render  $M$  pixels across the frame and minimize the loss

$$\mathcal{L}_{\text{map}} = \sum_{k=1}^M |D_k - \hat{D}_k|_1 + \lambda_m |I_k - \hat{I}_k|_1, \quad (5)$$

where  $\lambda_m$  is a hyperparameter.

**Keyframe Selection and Submap Initialization.** Creating submaps too often can increase pose drift, especially for trajectories with many small loops. Instead of using a fixed interval when creating the *global* keyframes as in [9, 13, 29],

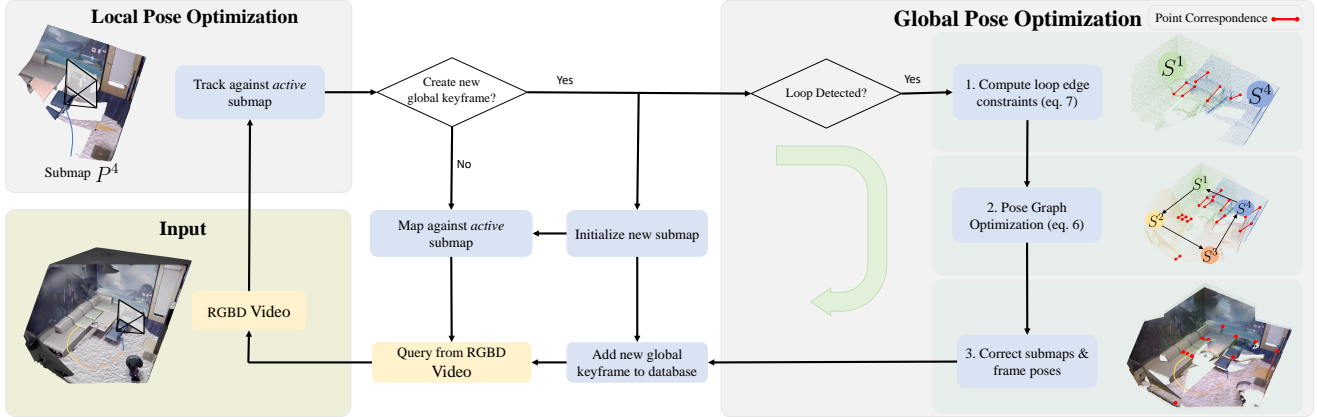


Figure 2. **Loopy-SLAM Overview.** Given an input RGBD stream, we first track the frame against the current *active* submap. If a new *global* keyframe is triggered from the estimated motion, we initialize a new submap, otherwise we continue mapping against the same submap. If a loop is detected between the just completed submap and the past *global* keyframes, pose graph optimization (PGO) is triggered. First, we compute the loop edge constraints (1) with a coarse to fine dense surface registration technique and then PGO (2) is performed with a robust dense surface registration objective. The poses and submaps are then rigidly corrected to achieve global pose and map alignment (3). Finally, the just triggered new *global* keyframe is added to the place recognition database.

we dynamically create global keyframes based on the camera motion [7, 52]. When the rotation angle to the *global* keyframe of the *active* submap exceeds a threshold  $\sigma$  or the relative translation exceeds  $\theta$ , we create a new submap. For each new submap  $P^s$ , to speed up the mapping process, we initialize it with the projection of the past neural point cloud submap  $P^{s-1}$  into the new *global* keyframe. Apart from the *global* keyframes, we also keep *local* keyframes which are generated at a regular interval within each submap to constrain the mapping as in [45], but on a per-submap basis, instead of on the global scene representation. These are deleted when a new submap is initialized.

### 3.2. Loop Closure and Refinement

Global place recognition is performed before starting a new submap to build edges in a pose graph. Loop closure edge constraints are computed using a coarse to fine registration strategy and the pose graph is optimized with a robust line process to reject outlier edge candidates. The output from the pose graph optimization (PGO) is a set of refined *global* keyframe poses which are used to correct all frame poses and map points belonging to each submap. At the end of trajectory capture, feature fusion and refinement are performed jointly on all submaps.

**Global Place Recognition.** To allow for the correction of arbitrary drifts we add every *global* keyframe to a bag of visual words (BoW) database [43] for global place recognition. Every time a *global* keyframe is created, it is added to the BoW database. This is in contrast to *e.g.* MIPS-Fusion [57] which detects loop closures via submap overlap, which is limited to the correction of smaller drifts.

**Pose Graph Optimization.** We build a pose graph by first defining each node  $T_s \in SE(3)$  as the correction to the

world coordinate pose of the *global* keyframe. We further populate odometry edges with identity constraints  $\{I_s\}$  between the adjacent keyframes of submaps  $P^s$  and  $P^{s+1}$ . Loop edge constraints  $\{T_{st}\} \in SE(3)$  are added between non-adjacent nodes by querying the BoW database when a submap has been completed. We query the top  $K$  neighbors from the BoW and add them as nodes in the pose graph if the visual similarity score is higher than a dynamically computed threshold  $s_{min}$ . The threshold  $s_{min}$  is the minimum score between the *global* keyframe and the frames of the associated submap. PGO is triggered in an online fashion to mitigate real-time inter-submap drift, which is critical to be resolved as early as possible. We use a robust PGO strategy based on dense surface registration which filters outlier loop edges during optimization, following [9]. We choose a dense surface registration objective since it is inherently tied to the local submaps which we aim to correct, in contrast to the relative pose residual used in *e.g.* [34]. To be robust against erroneous loop edges, a line process  $\mathbb{L} = \{l_{st}\}$  is added as a jointly optimized weight ( $l_{st} \in [0, 1]$ ) over the loop edges. We optimize the *global* keyframe pose corrections  $\mathbb{T} = \{T_s\}$  along with the loop weights  $\mathbb{L}$  by minimizing the objective

$$\mathbb{E}(\mathbb{T}, \mathbb{L}) = \sum_s f(T_s, T_{s+1}, I_s) + \lambda \left( \sum_{s,t} l_{st} f(T_s, T_t, T_{st}) + \mu \sum_{s,t} (\sqrt{l_{st}} - 1)^2 \right), \quad (6)$$

where  $\lambda$  and  $\mu$  are hyperparameters. The dense surface registration terms  $f(T_s, T_t, X)$  are defined as the sum of squared distances between corresponding points in submaps

$P^s$  and  $P^t$

$$f(T_s, T_t, X) = \sum_{(p,q)} \|T_s p - T_t q\|^2 \\ \approx \sum_p \|T_s p - T_t X p\|^2, \quad (7)$$

where  $(p, q)$  defines the set of corresponding points. The last term in Eq. (6) is a regularizer to prevent the trivial solution. The objective is optimized with Levenberg-Marquardt. For more details, we refer to Choi *et al.* [9]. We initialize  $\mathbb{T}$  to identity and follow a two-stage optimization where, in a first stage, loop edges with  $l_{st} < l_{min}$  are removed. In a second stage, all remaining loop edges are used. The output from the PGO is a set of rigid correction terms  $\mathbb{T}$  to the *global* keyframe poses. We apply  $\mathbb{T}$  to the keyframe world coordinate poses and the frame poses associated with the submaps, as well as the submaps themselves.

**Loop Edge Constraints.** For every loop edge in the pose graph between submaps  $P^s$  and  $P^t$ , the constraints  $T_{st}$  need to be computed. We use a coarse to fine dense registration technique to align the source and target submaps. We found that using the neural point cloud submaps  $P^s$  directly was inherently unstable for two reasons: 1) dense surface registration methods need uniformly drawn samples on the surface, but the submaps  $P^s$  have a dynamic resolution, 2) the anchored points in  $P^s$  come from a single depth observation, which may be noisy and can corrupt the surface registration. To mitigate these two effects, we suppress noise by integrating all depth frames associated with a submap with volumetric TSDF Fusion [11] and sample uniformly drawn points from the surface extracted by marching cubes [27]. Denote the point clouds extracted by volumetric fusion from submaps  $P^s$  and  $P^t$  as  $S^s$  and  $S^t$  respectively. As coarse alignment we use the global registration method of Rusu *et al.* [42] which extracts Fast Point Feature Histograms (FPFH) features for each point from down sampled versions of the source  $S^s$  and target  $S^t$  point clouds. Correspondence search is then performed in the FPFH feature space rather than in Euclidean 3-space. The optimization is wrapped in a RANSAC framework to reject outlier correspondences and the output is a rigid correction to the source point cloud  $S^s$  such that it aligns with the target  $S^t$ . To refine the estimate, ICP is used on the full resolution point clouds. Finally, though the PGO has built in outlier handling, we find it useful to prefilter the loop edges based on the quality of the constraints. Specifically, we find a strong correlation between the error of the constraint and the translation magnitude of the constraint. We therefore remove edges with a translation constraint magnitude above a dynamically computed threshold  $t_{min}$ . We compute the threshold  $t_{min}$  based on statistics from all loop constraints by using a percentile that yields a standard deviation on the remaining loop edges below a threshold  $\sigma_{min}$ . Addition-

ally, we require that the so called fitness score, which measures the overlapping area ( $\#$  of inlier correspondences /  $\#$  of points in target), to be above a threshold  $f_{min}$ .

**Feature Fusion and Refinement.** At the end of the trajectory capture, we concatenate all submaps to a global neural point cloud from which a global 3D model can be extracted. During concatenation, we first perform feature fusion in the overlapping submap regions to compress the model. Concretely, thanks to the projective initialization strategy when creating new submaps, point correspondences between submaps come for free. Note that these neural point correspondences are not the same as those between the point cloud correspondences in Eq. (7), which are used to compute the loop edge constraints. The submaps  $P^s$  create a chain of correspondences and corresponding points can thus exist between more than two submaps. The correspondences are averaged in terms of location and features *i.e.* we compute the average as  $\bar{p}_i = \sum_s p_i^s / |s|$ ,  $\bar{f}_i^g = \sum_s f_i^{s,g} / |s|$  and  $\bar{f}_i^c = \sum_s f_i^{s,c} / |s|$ , where we sum over the relevant submaps for each point  $i$  which has correspondences.  $|s|$  denotes the cardinality of the set of submaps we sum over.

After feature fusion, we perform a set of refinements steps on the global neural point cloud. During this step, we use the *global* keyframes and optimize the color and geometric features using a fixed color decoder  $g_\xi$ .

## 4. Experiments

We describe our experimental setup and then evaluate our method against state-of-the-art dense neural RGBD SLAM methods on Replica [51] as well as the real world TUM-RGBD [53] and the ScanNet [12] datasets. For more experiments and details, we refer to the supplementary material.

**Implementation Details.** For *global* keyframe selection we use  $\theta = 0.3m$  and  $\sigma = 20^\circ$  on Replica and ScanNet. On TUM-RGBD, we use  $\theta = 0.45m$  and  $\sigma = 30^\circ$ . For the loop closure specific parameters, we add the top  $K = 4$  queries from the BoW for Replica and  $K = 1$  for ScanNet and TUM-RGBD. To pre-filter loop edges, we use  $\sigma_{min} = 0.15$  and  $f_{min} = 0.1$  for ScanNet and TUM-RGBD. For Replica, no pre-filtering is performed. To prune the loop edges, we use  $l_{min} = 0.25$  on Replica and Scannet while we use  $l_{min} = 0.1$  on TUM-RGBD. Following [9], we use  $\mu = 0.04\kappa$ , where  $\kappa$  is the average cardinality of the two correspondence sets  $\mathcal{K}_{ij}$  and  $\mathcal{K}_{ji}$ . Here  $\mathcal{K}_{ij}$  is the set of correspondences between  $X S^i$  and  $S^j$  that are within distance  $\epsilon = 0.05$  m. We use  $\lambda = 5$  for all experiments. For the tracking and mapping specific hyperparameters as well as meshing, we follow [45], *i.e.* we render depth and color every fifth frame over the estimated trajectory and use TSDF Fusion [11] with voxel size 1 cm. We use  $\lambda_t = 0.5$  and  $\lambda_m = 0.1$  for the color weight in the tracking and mapping loss respectively. For tracking, we sample  $M_t = 1.5K$

Method	LC	Rm 0	Rm 1	Rm 2	OFF 0	OFF 1	OFF 2	OFF 3	OFF 4	Avg.
NICE-SLAM [77]	✗	0.97	1.31	1.07	0.88	1.00	1.06	1.10	1.13	1.06
Vox-Fusion [73]	✗	1.37	4.70	1.47	8.48	2.04	2.58	1.11	2.94	3.09
ESLAM [28]	✗	0.71	0.70	0.52	0.57	0.55	0.58	0.72	<b>0.63</b>	0.63
Point-SLAM [45]	✗	0.61	0.41	0.37	0.38	0.48	0.54	0.69	0.72	0.52
MIPS-Fusion [57]	✓	1.10	1.20	1.10	0.70	0.80	1.30	2.20	1.10	1.19
GO-SLAM [76]	✓	0.34	0.29	0.29	0.32	<b>0.30</b>	0.39	0.39	0.46	0.35
<b>Ours</b>	✓	<b>0.24</b>	<b>0.24</b>	<b>0.28</b>	<b>0.26</b>	0.40	<b>0.29</b>	<b>0.22</b>	<b>0.35</b>	<b>0.29</b>

Table 1. **Tracking Performance on Replica [51]** (ATE RMSE ↓ [cm]). For all but one scene, we achieve more accurate tracking than existing methods. LC indicates loop closure. The best results are highlighted as **first**, **second**, and **third**.

(K=kilo) pixels uniformly on Replica. On TUM-RGBD and ScanNet, we first compute the top 75K pixels based on the image gradient magnitude and sample  $M_t = 5K$  out of this set. For mapping, we sample uniformly  $M = 5K$  pixels for Replica and 10K pixels for TUM-RGBD and ScanNet. See the supplementary material for more details.

**Evaluation Metrics.** The meshes are extracted with marching cubes [27] and evaluated using the F-score which is the harmonic mean of the Precision and Recall. A distance threshold of 1 cm is used for all evaluations. We also provide the depth L1 metric which evaluates the depth on the mesh at random poses against its ground truth. For tracking accuracy, we use ATE RMSE [53] and for rendering we report the peak signal-to-noise ratio (PSNR), SSIM [64] and LPIPS [75]. Our rendering metrics are evaluated by rendering the full resolution image along the estimated trajectory every 5th frame. Unless otherwise written, we report the average metric of three runs.

**Datasets.** The Replica dataset [51] consists of high-quality 3D reconstructions of diverse indoor scenes. We leverage the publicly available dataset by Sucar *et al.* [54], which contains trajectories from an RGBD sensor. Additionally, we showcase our framework on real-world data using the TUM-RGBD dataset [53] and the ScanNet dataset [12]. The TUM-RGBD poses were captured utilizing an external motion capture system, while ScanNet uses poses from BundleFusion [13].

**Baseline Methods.** We primarily compare our method to existing state-of-the-art dense neural RGBD SLAM methods such as ESLAM [28], Point-SLAM [45] and GO-SLAM [76]. We use the numbers from the respective papers where available. Otherwise, we reproduce them ourselves.

#### 4.1. Reconstruction

Fig. 3a compares our method to state-of-the-art dense RGBD neural SLAM methods in terms of the geometric reconstruction accuracy. We outperform all methods on the majority of scenes and report an average improvement of 20% and 70% to the second (Point-SLAM) and third (ESLAM) best performing methods on the depth L1 metric. Fig. 3b compares the mesh reconstructions of ESLAM [28],

Method	LC	fr1/ desk	fr1/ desk2	fr1/ room	fr2/ xyz	fr3/ office	Avg.
DI-Fusion [21]	✗	4.4	N/A	N/A	2.0	5.8	N/A
NICE-SLAM [77]	✗	4.26	4.99	34.49	6.19	3.87	10.76
Vox-Fusion [73]	✗	3.52	6.00	19.53	1.49	26.01	11.31
MIPS-Fusion [57]	✓	3.0	N/A	N/A	1.4	4.6	N/A
Point-SLAM [45]	✗	4.34	4.54	30.92	1.31	3.48	8.92
ESLAM [28]	✗	2.47	3.69	29.73	1.11	2.42	7.89
Co-SLAM [61]	✗	2.40	N/A	N/A	1.7	2.4	N/A
GO-SLAM [76]	✓	<b>1.5</b>	N/A	<b>4.64</b>	<b>0.6</b>	1.3	N/A
<b>Ours</b>	✓	3.79	3.38	7.03	1.62	3.41	<b>3.85</b>
BAD-SLAM [48]	✓	1.7	N/A	N/A	1.1	1.7	N/A
Kintinuous [69]	✓	3.7	7.1	7.5	2.9	3.0	4.84
ORB-SLAM2 [34]	✓	1.6	<b>2.2</b>	4.7	<b>0.4</b>	1.0	<b>1.98</b>
ElasticFusion [71]	✓	2.53	6.83	21.49	1.17	2.52	6.91
BundleFusion [13]	✓	1.6	N/A	N/A	1.1	2.2	N/A
Cao <i>et al.</i> [7]	✓	<b>1.5</b>	N/A	N/A	<b>0.6</b>	<b>0.9</b>	N/A
Yan <i>et al.</i> [72]	✓	1.6	N/A	5.1	N/A	3.1	N/A

Table 2. **Tracking Performance on TUM-RGBD [53]** (ATE RMSE ↓ [cm]). Loopy-SLAM shows competitive performance on a variety of scenes. On average Loopy-SLAM outperforms existing dense neural RGBD methods (top part) that do not employ loop closure (LC), and is reducing the gap to traditional dense and sparse SLAM methods (bottom part).

Method	00	59	106	169	181	207	54	233	465	Avg.-6	Avg.-9
Vox-Fusion [73]	16.6	24.2	8.4	27.3	23.3	9.4	-	-	-	18.5	-
Co-SLAM [61]	7.1	11.1	9.4	<b>5.9</b>	11.8	7.1	-	-	-	8.8	-
MIPS-Fusion [57]	7.9	10.7	9.7	9.7	14.2	7.8	-	-	-	10.0	-
NICE-SLAM [77]	12.0	14.0	7.9	10.9	13.4	6.2	20.9	9.0	22.3	10.7	13.0
ESLAM [28]	7.3	8.5	7.5	6.5	9.0	<b>5.7</b>	36.3	<b>4.3</b>	16.5	7.4	11.3
Point-SLAM [45]	10.2	7.8	8.7	22.2	14.8	9.5	28.0	6.1	21.6	12.2	14.3
GO-SLAM [76]	5.4	<b>7.5</b>	<b>7.0</b>	7.7	<b>6.8</b>	6.9	8.8	4.8	<b>8.2</b>	<b>6.9</b>	<b>7.0</b>
<b>Ours</b>	<b>4.2</b>	<b>7.5</b>	8.3	7.5	10.6	7.9	<b>7.5</b>	5.2	10.9	7.7	7.7

Table 3. **Tracking Performance on ScanNet [12]** (ATE RMSE ↓ [cm]). Loopy-SLAM yields competitive performance on a variety of scenes. Avg.-6 and Avg.-9 means averaging over the 6 and 9 scenes respectively.

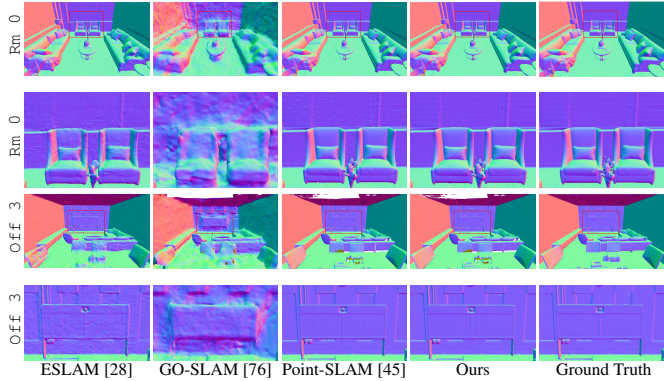
Metric	NICE-SLAM[77]	Vox-Fusion[73]	ESLAM [28]	Point-SLAM[45]	Ours
PSNR [dB] ↑	24.42	24.41	27.8	35.17	<b>35.47</b>
SSIM ↑	0.809	0.801	0.921	0.975	<b>0.981</b>
LPIPS ↓	0.233	0.236	0.245	0.124	<b>0.109</b>

Table 4. **Rendering Performance on Replica [51].** We marginally outperform Point-SLAM on the commonly reported rendering metrics. Otherwise, we outperform existing methods like NICE-SLAM, Vox-Fusion and ESLAM. Results are averaged over all 8 scenes.

GO-SLAM [76], Point-SLAM [45] and our method to the ground truth mesh. We find that our method is able to resolve fine details to a significant extent, even beating Point-SLAM on detailed geometry (see the zoomed in visualizations). We attribute this to our online loop closure strategy which globally optimizes the poses and submaps globally. Finally, in Fig. 4 we qualitatively evaluate on ScanNet, showing improvements in geometric accuracy over ESLAM

Method	Metric	Rm0	Rm1	Rm2	Off0	Off1	Off2	Off3	Off4	Avg.
NICE-SLAM [77]	Depth L1 [cm] ↓	1.81	1.44	2.04	1.39	1.76	8.33	4.99	2.01	2.97
	F1 [%] ↑	45.0	44.8	43.6	50.0	51.9	39.2	39.9	36.5	43.9
Vox-Fusion [73]	Depth L1 [cm] ↓	1.09	1.90	2.21	2.32	3.40	4.19	2.96	1.61	2.46
	F1 [%] ↑	69.9	34.4	59.7	46.5	40.8	51.0	64.6	50.7	52.2
ESLAM [28]	Depth L1 [cm] ↓	0.97	1.07	1.28	0.86	1.26	1.71	1.43	1.06	1.18
	F1 [%] ↑	81.0	82.2	83.9	78.4	75.5	77.1	75.5	79.1	79.1
Co-SLAM [61]	Depth L1 [cm] ↓	1.05	0.85	2.37	1.24	1.48	1.86	1.66	1.54	1.51
	Depth L1 [cm] ↓	-	-	-	-	-	-	-	-	3.38
GO-SLAM [76]	*Depth L1 [cm] ↓	4.56	1.97	3.43	2.47	3.03	10.3	7.31	4.34	4.68
	F1 [%] ↑	17.3	33.4	24.0	43.0	31.8	21.8	17.3	22.0	26.3
Point-SLAM [45]	Depth L1 [cm] ↓	0.53	0.22	0.46	0.30	0.57	0.49	0.51	0.46	0.44
	F1 [%] ↑	86.9	92.3	90.8	93.8	91.6	89.0	88.2	85.6	89.8
<b>Ours</b>	Depth L1 [cm] ↓	<b>0.30</b>	<b>0.20</b>	<b>0.42</b>	<b>0.23</b>	<b>0.46</b>	<b>0.60</b>	<b>0.37</b>	<b>0.24</b>	<b>0.35</b>
	F1 [%] ↑	<b>91.6</b>	<b>92.4</b>	<b>90.6</b>	<b>93.9</b>	<b>91.6</b>	<b>88.5</b>	<b>89.0</b>	<b>88.7</b>	<b>90.8</b>

(a)



(b)

Figure 3. **Reconstruction Performance on Replica [51]**. Fig. 3a: Our method performs better than all existing methods on average. Fig. 3b: Compared to ESSLAM which uses axis aligned feature planes and GO-SLAM which uses multi-resolution hash grids, Loopy-SLAM has a significant advantage in terms of the accuracy of the reconstructions due to the neural point cloud of dynamic resolution. Moreover, with the pose accuracy we obtain via loop closure, we close the gap to the ground truth further. See specifically the zoomed in visualizations. \*Depth L1 for GO-SLAM shows our reproduced results from random poses (GO-SLAM evaluates on ground truth poses).

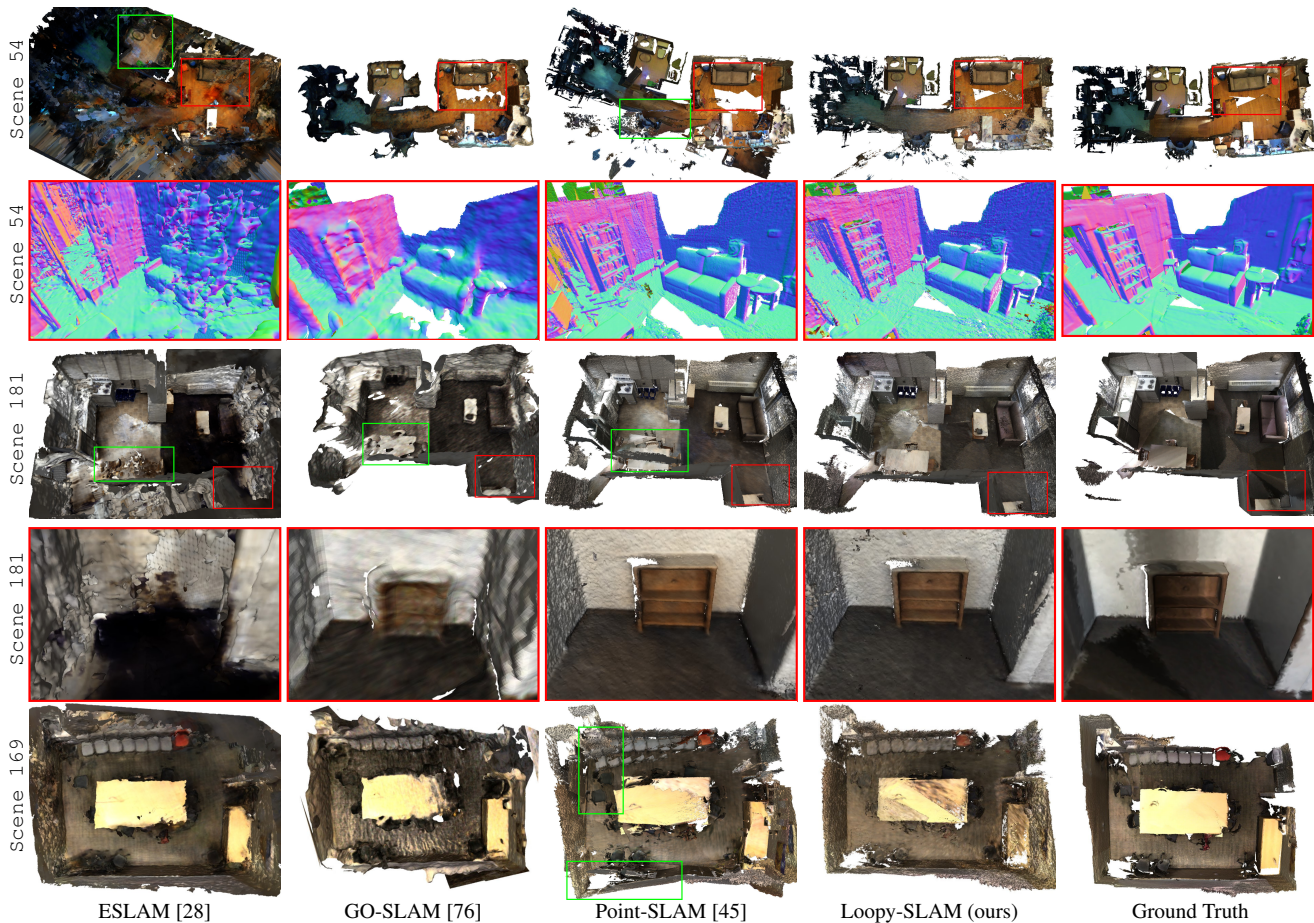


Figure 4. **Mesh Evaluation on ScanNet [12]**. Loopy-SLAM yields drift free large scale reconstructions compared to Point-SLAM (scene 54, scene 181, scene 169) and ESSLAM (scene 54) and with more accurate geometry compared to GO-SLAM (all scenes) and ESSLAM (scene 54, scene 181). The green boxes highlight drifted or poor geometry. The red boxes show the zoomed in view locations.

and GO-SLAM and over Point-SLAM due to more accurate pose estimates.

## 4.2. Tracking

We report the tracking performance on the Replica dataset in Tab. 1. We outperform the existing methods on all scenes except one. We attribute this to robust frame-to-model local pose estimation coupled with our pose graph optimization which globally aligns the submap frames. We further show competitive performance on real-world data by evaluating on the TUM-RGBD and ScanNet datasets in Tab. 2 and Tab. 3 respectively. On both datasets, among the dense neural SLAM methods, we are competitive compared to GO-SLAM [76] while beating all other dense neural SLAM methods on average. The `fr1 room` and `scene 54` scenes highlights the importance of incorporating loop closure - the best method without loop closure achieves an ATE RMSE of 19.53 cm on the `fr1 room` scene while GO-SLAM and our method can reduce this significantly. Encouragingly, Loopy-SLAM shows state-of-the art performance on `scene 54` which is the only multi-room scene and the largest scene in terms of spatial extent. We show mesh evaluations on ScanNet in Fig. 4 which further emphasizes the need for online loop closure compared to ES-LAM and Point-SLAM.

## 4.3. Rendering

Tab. 4 compares rendering performance on the Replica dataset and shows competitive performance to Point-SLAM [45], beating NICE-SLAM [77], Vox-Fusion [73] and ESLAM [28]. Unfortunately, the rendering code for GO-SLAM [76] did not work at the time of submission.

## 4.4. Further Statistical Evaluation

**Memory and Runtime Analysis.** Tab. 5 shows the runtime and memory usage of our method. Our memory usage is competitive and we can run all experiments on a 12 GB GPU card. GO-SLAM [76] and ESLAM [28] typically need a 24 GB card. Our mapping and tracking runtime is equivalent to Point-SLAM [45] (excluding loop closure) and implemented with Pytorch. On `fr1 desk` we report 7 PGOs taking on average 1 ms/PGO and requiring on average 8 registrations/PGO which on average take 12 sec/registration. Note that all registrations but the ones belonging to the *active* submap can be computed in parallel while mapping the *active* submap. The registrations to the *active* submap can be computed while mapping the next submap.

**Number of Scene Points.** Tab. 6 compares the number of total neural scene points on the TUM-RGBD dataset. Loopy-SLAM yields on average 14 % more scene points with the advantage of a 57 % gain in the ATE RMSE.

**Limitations.** While our proposed method shows competitive performance in terms of tracking on real-world data, we

Method	Tracking /Iteration	Mapping /Iteration	Tracking /Frame	Mapping /Frame	Decoder Size	Embedding Size
NICE-SLAM [77]	32 ms	182 ms	1.32 s	10.92 s	0.47 MB	95.86 MB
Vox-Fusion [73]	<b>12 ms</b>	55 ms	0.36 s	0.55 s	1.04 MB	<b>0.149 MB</b>
Point-SLAM [45]	21 ms	33 ms	0.85 s	9.85 s	0.51 MB	27.23 MB
ESLAM [28]	15 ms	<b>29 ms</b>	0.12 s	0.44 s	<b>0.01 MB</b>	45.46 MB
GO-SLAM [76]	-	-	0.85 s	9.85 s	0.04 MB	48.07 MB
<b>Ours</b>	21 ms	33 ms	0.85 s	9.85 s	0.51 MB	60.92 MB

Table 5. **Runtime and Memory Usage on Replica** `office 0`. The decoder size is the memory of all MLP networks. The embedding size is the total memory of the map representation. Memory usage is competitive. It can be noted that GO-SLAM needs an extra 15.28 MB for their tracker.

Method	fr1/ desk	fr1/ desk2	fr1/ xyz	fr2/ room	fr3/ office	Avg.	Avg. ATE
Point-SLAM [45]	<b>65K</b>	<b>102K</b>	51K	<b>288K</b>	<b>303K</b>	<b>162K</b>	8.92 cm
<b>Ours</b>	93K	162K	<b>49K</b>	298K	316K	184K	<b>3.85 cm</b>

Table 6. **Number of Scene Points on TUM-RGBD [53]**. Compared to Point-SLAM, Loopy-SLAM yields on average 14 % more points in the scene representation. This is a relatively small gain in footprint from the submap creation and loop closure strategy which bring a 57 % improvement in terms of the ATE RMSE.

believe that a more robust tracker can be built with a combination of frame-to-model and frame-to-frame queues. We also believe that more robust and faster registrations can be obtained by making use of not only 3D point features, but also image features from the associated keyframes. Place recognition can likely be improved with learned variants. Currently, our implementation is using Pytorch and Open3D via python bindings and not optimized for real-time operation. To improve runtime many parts of the method should benefit from a direct CUDA implementation instead. Finally, our system does not implement relocalization, which is an important part of a robust SLAM system. We leave these things for future work.

## 5. Conclusion

We proposed Loopy-SLAM, a dense RGBD SLAM system which utilizes submaps of neural point clouds for local mapping and tracking and a pose graph for global pose and map optimization. The underlying point based representation allows for local map updates by shifting the points, contrary to re-integration strategies seen in previous works which requires that all mapped frames are stored during runtime. In comparison, our submap based integration strategy has the potential for better scalability. Our experiments show that Loopy-SLAM leverages the benefit of the neural point cloud representation and equips it with loop closure to demonstrate state-of-the art dense reconstruction performance as well as competitive tracking and rendering accuracy to existing methods.

**Acknowledgements.** This work was supported by a VIVO collaboration project on real-time scene reconstruction and research grants from FIFA. We thank Manthan Patel for fruitful discussions.



## References

- [1] Voxgraph: Globally consistent, volumetric mapping using signed distance function submaps. *IEEE Robotics and Automation Letters*, 5(1):227–234, 2019.
- [2] Dejan Azinović, Ricardo Martin-Brualla, Dan B Goldman, Matthias Nießner, and Justus Thies. Neural rgb-d surface reconstruction. In *IEEE/CVF Conference on Computer Vision and Pattern Recognition*, pages 6290–6301, 2022.
- [3] Wenjing Bian, Zirui Wang, Kejie Li, Jia-Wang Bian, and Victor Adrian Prisacariu. Nope-nerf: Optimising neural radiance field with no pose prior. *arXiv preprint arXiv:2212.07388*, 2022.
- [4] Michael Bosse, Paul Newman, John Leonard, Martin Soika, Wendelin Feiten, and Seth Teller. An atlas framework for scalable mapping. In *2003 IEEE International Conference on Robotics and Automation (Cat. No. 03CH37422)*, pages 1899–1906. IEEE, 2003.
- [5] Aljaž Božič, Pablo Palafox, Justus Thies, Angela Dai, and Matthias Nießner. Transformerfusion: Monocular rgb scene reconstruction using transformers. *arXiv preprint arXiv:2107.02191*, 2021.
- [6] E. Bylow, C. Olsson, and F. Kahl. Robust online 3d reconstruction combining a depth sensor and sparse feature points. In *2016 23rd International Conference on Pattern Recognition (ICPR)*, pages 3709–3714, 2016.
- [7] Yan-Pei Cao, Leif Kobbelt, and Shi-Min Hu. Real-time high-accuracy three-dimensional reconstruction with consumer rgb-d cameras. *ACM Transactions on Graphics (TOG)*, 37(5):1–16, 2018.
- [8] Jaesung Choe, Sunghoon Im, Francois Rameau, Minjun Kang, and In So Kweon. Volumefusion: Deep depth fusion for 3d scene reconstruction. In *IEEE/CVF International Conference on Computer Vision (ICCV)*, pages 16086–16095, 2021.
- [9] Sungjoon Choi, Qian-Yi Zhou, and Vladlen Koltun. Robust reconstruction of indoor scenes. In *Proceedings of the IEEE conference on computer vision and pattern recognition*, pages 5556–5565, 2015.
- [10] Chi-Ming Chung, Yang-Che Tseng, Ya-Ching Hsu, Xiang-Qian Shi, Yun-Hung Hua, Jia-Fong Yeh, Wen-Chin Chen, Yi-Ting Chen, and Winston H Hsu. Orbeez-slam: A real-time monocular visual slam with orb features and nerf-realized mapping. *arXiv preprint arXiv:2209.13274*, 2022.
- [11] Brian Curless and Marc Levoy. Volumetric method for building complex models from range images. In *SIGGRAPH Conference on Computer Graphics*. ACM, 1996.
- [12] Angela Dai, Angel X. Chang, Manolis Savva, Maciej Halber, Thomas Funkhouser, and Matthias Nießner. ScanNet: Richly-annotated 3D reconstructions of indoor scenes. In *Conference on Computer Vision and Pattern Recognition (CVPR)*. IEEE/CVF, 2017.
- [13] Angela Dai, Matthias Nießner, Michael Zollhöfer, Shahram Izadi, and Christian Theobalt. Bundlefusion: Real-time globally consistent 3d reconstruction using on-the-fly surface reintegration. *ACM Transactions on Graphics (ToG)*, 36(4):1, 2017.
- [14] Felix Endres, Jürgen Hess, Nikolas Engelhard, Jürgen Sturm, Daniel Cremers, and Wolfram Burgard. An evaluation of the rgb-d slam system. In *2012 IEEE international conference on robotics and automation*, pages 1691–1696. IEEE, 2012.
- [15] Jakob Engel, Thomas Schöps, and Daniel Cremers. Lsdslam: Large-scale direct monocular slam. In *European conference on computer vision*, pages 834–849. Springer, 2014.
- [16] Nicola Fioraio, Jonathan Taylor, Andrew Fitzgibbon, Luigi Di Stefano, and Shahram Izadi. Large-scale and drift-free surface reconstruction using online subvolume registration. In *Proceedings of the IEEE Conference on Computer Vision and Pattern Recognition*, pages 4475–4483, 2015.
- [17] Peter Henry, Michael Krainin, Evan Herbst, Xiaofeng Ren, and Dieter Fox. Rgb-d mapping: Using kinect-style depth cameras for dense 3d modeling of indoor environments. *The international journal of Robotics Research*, 31(5):647–663, 2012.
- [18] Peter Henry, Dieter Fox, Achintya Bhowmik, and Rajiv Mongia. Patch volumes: Segmentation-based consistent mapping with rgb-d cameras. In *2013 International Conference on 3D Vision-3DV 2013*, pages 398–405. IEEE, 2013.
- [19] Berthold KP Horn, Hugh M Hilden, and Shahriar Negahdaripour. Closed-form solution of absolute orientation using orthonormal matrices. *JOSA A*, 5(7):1127–1135, 1988.
- [20] Armin Hornung, Kai M Wurm, Maren Bennewitz, Cyrill Stachniss, and Wolfram Burgard. Octomap: An efficient probabilistic 3d mapping framework based on octrees. *Autonomous robots*, 34:189–206, 2013.
- [21] Jiahui Huang, Shi-Sheng Huang, Haoxuan Song, and Shi-Min Hu. Di-fusion: Online implicit 3d reconstruction with deep priors. In *IEEE/CVF Conference on Computer Vision and Pattern Recognition*, pages 8932–8941, 2021.
- [22] Olaf Kähler, Victor Adrian Prisacariu, Carl Yuheng Ren, Xin Sun, Philip H. S. Torr, and David William Murray. Very high frame rate volumetric integration of depth images on mobile devices. *IEEE Trans. Vis. Comput. Graph.*, 21(11):1241–1250, 2015.
- [23] Olaf Kähler, Victor A Prisacariu, and David W Murray. Real-time large-scale dense 3d reconstruction with loop closure. In *Computer Vision—ECCV 2016: 14th European Conference, Amsterdam, The Netherlands, October 11–14, 2016, Proceedings, Part VIII 14*, pages 500–516. Springer, 2016.
- [24] Christian Kerl, Jürgen Sturm, and Daniel Cremers. Dense visual slam for rgb-d cameras. In *2013 IEEE/RSJ International Conference on Intelligent Robots and Systems*, pages 2100–2106. IEEE, 2013.
- [25] Heng Li, Xiaodong Gu, Weihao Yuan, Luwei Yang, Zilong Dong, and Ping Tan. Dense rgb slam with neural implicit maps. *arXiv preprint arXiv:2301.08930*, 2023.
- [26] Chen Hsuan Lin, Wei Chiu Ma, Antonio Torralba, and Simon Lucey. BARF: Bundle-Adjusting Neural Radiance Fields. In *International Conference on Computer Vision (ICCV)*. IEEE/CVF, 2021.
- [27] William E Lorensen and Harvey E Cline. Marching cubes: A high resolution 3d surface construction algorithm. *ACM siggraph computer graphics*, 21(4):163–169, 1987.

- [28] Mohammad Mahdi Johari, Camilla Carta, and François Fleuret. Eslam: Efficient dense slam system based on hybrid representation of signed distance fields. *arXiv e-prints*, pages arXiv–2211, 2022.
- [29] Robert Maier, Jürgen Sturm, and Daniel Cremers. Submap-based bundle adjustment for 3d reconstruction from rgb-d data. In *Pattern Recognition: 36th German Conference, GCPR 2014, Münster, Germany, September 2-5, 2014, Proceedings 36*, pages 54–65. Springer, 2014.
- [30] R Maier, R Schaller, and D Cremers. Efficient online surface correction for real-time large-scale 3d reconstruction. *arXiv preprint arXiv:1709.03763*, 2017.
- [31] Hidenobu Matsuki, Keisuke Tateno, Michael Niemeyer, and Federic Tombari. Newton: Neural view-centric mapping for on-the-fly large-scale slam. *arXiv preprint arXiv:2303.13654*, 2023.
- [32] Ben Mildenhall, Pratul P. Srinivasan, Matthew Tancik, Jonathan T. Barron, Ravi Ramamoorthi, and Ren Ng. NeRF: Representing Scenes as Neural Radiance Fields for View Synthesis. In *European Conference on Computer Vision (ECCV)*. CVF, 2020.
- [33] Thomas Müller, Alex Evans, Christoph Schied, and Alexander Keller. Instant neural graphics primitives with a multiresolution hash encoding. *ACM Transactions on Graphics (ToG)*, 41(4):1–15, 2022.
- [34] Raul Mur-Artal and Juan D. Tardos. ORB-SLAM2: An Open-Source SLAM System for Monocular, Stereo, and RGB-D Cameras. *IEEE Transactions on Robotics*, 33(5): 1255–1262, 2017.
- [35] Zak Murez, Tarrence van As, James Bartolozzi, Ayan Sinha, Vijay Badrinarayanan, and Andrew Rabinovich. Atlas: End-to-end 3d scene reconstruction from posed images. In *Computer Vision—ECCV 2020: 16th European Conference, Glasgow, UK, August 23–28, 2020, Proceedings, Part VII 16*, pages 414–431. Springer, 2020.
- [36] Richard A Newcombe, Shahram Izadi, Otmar Hilliges, David Molyneaux, David Kim, Andrew J Davison, Pushmeet Kohli, Jamie Shotton, Steve Hodges, and Andrew W Fitzgibbon. Kinectfusion: Real-time dense surface mapping and tracking. In *ISMAR*, pages 127–136, 2011.
- [37] Matthias Nießner, Michael Zollhöfer, Shahram Izadi, and Marc Stamminger. Real-time 3d reconstruction at scale using voxel hashing. *ACM Transactions on Graphics (TOG)*, 32, 2013.
- [38] Michael Oechsle, Songyou Peng, and Andreas Geiger. UNISURF: Unifying Neural Implicit Surfaces and Radiance Fields for Multi-View Reconstruction. In *International Conference on Computer Vision (ICCV)*. IEEE/CVF, 2021.
- [39] Helen Oleynikova, Zachary Taylor, Marius Fehr, Roland Siegwart, and Juan I. Nieto. Voxblox: Incremental 3d euclidean signed distance fields for on-board MAV planning. In *2017 IEEE/RSJ International Conference on Intelligent Robots and Systems, IROS 2017, Vancouver, BC, Canada, September 24–28, 2017*, pages 1366–1373. IEEE, 2017.
- [40] Joseph Ortiz, Alexander Clegg, Jing Dong, Edgar Sucar, David Novotny, Michael Zollhoefer, and Mustafa Mukadam. isdf: Real-time neural signed distance fields for robot perception. *arXiv preprint arXiv:2204.02296*, 2022.
- [41] Antoni Rosinol, John J. Leonard, and Luca Carlone. NeRF-SLAM: Real-Time Dense Monocular SLAM with Neural Radiance Fields. *arXiv*, 2022.
- [42] Radu Bogdan Rusu, Nico Blodow, and Michael Beetz. Fast point feature histograms (fpfh) for 3d registration. In *2009 IEEE international conference on robotics and automation*, pages 3212–3217. IEEE, 2009.
- [43] Rafael Muñoz Salinas. DBoW3 dbow3, 2017.
- [44] Erik Sandström, Martin R. Oswald, Suryansh Kumar, Silvan Weder, Fisher Yu, Cristian Sminchisescu, and Luc Van Gool. Learning Online Multi-Sensor Depth Fusion. In *European Conference Computer Vision (ECCV)*. CVF, 2022.
- [45] Erik Sandström, Yue Li, Luc Van Gool, and Martin R Oswald. Point-slam: Dense neural point cloud-based slam. In *International Conference on Computer Vision (ICCV)*. IEEE/CVF, 2023.
- [46] Erik Sandström, Kevin Ta, Luc Van Gool, and Martin R Oswald. Uncle-slam: Uncertainty learning for dense neural slam. In *International Conference on Computer Vision Workshops (ICCVW)*. IEEE/CVF, 2023.
- [47] Mohamed Sayed, John Gibson, Jamie Watson, Victor Prisacariu, Michael Firman, and Clément Godard. Simplerecon: 3d reconstruction without 3d convolutions. In *European Conference on Computer Vision*, pages 1–19. Springer, 2022.
- [48] Thomas Schops, Torsten Sattler, and Marc Pollefeys. BAD SLAM: Bundle adjusted direct RGB-D SLAM. In *CVF/IEEE Conference on Computer Vision and Pattern Recognition (CVPR)*, 2019.
- [49] Frank Steinbrucker, Christian Kerl, and Daniel Cremers. Large-scale multi-resolution surface reconstruction from rgb-d sequences. In *IEEE International Conference on Computer Vision*, pages 3264–3271, 2013.
- [50] Noah Stier, Alexander Rich, Pradeep Sen, and Tobias Höllerer. Vortex: Volumetric 3d reconstruction with transformers for voxelwise view selection and fusion. In *2021 International Conference on 3D Vision (3DV)*, pages 320–330. IEEE, 2021.
- [51] Julian Straub, Thomas Whelan, Lingni Ma, Yufan Chen, Erik Wijmans, Simon Green, Jakob J Engel, Raul Mur-Artal, Carl Ren, Shobhit Verma, et al. The replica dataset: A digital replica of indoor spaces. *arXiv preprint arXiv:1906.05797*, 2019.
- [52] Jörg Stückler and Sven Behnke. Multi-resolution surfel maps for efficient dense 3d modeling and tracking. *Journal of Visual Communication and Image Representation*, 25(1):137–147, 2014.
- [53] Jürgen Sturm, Nikolas Engelhard, Felix Endres, Wolfram Burgard, and Daniel Cremers. A benchmark for the evaluation of RGB-D SLAM systems. In *International Conference on Intelligent Robots and Systems (IROS)*. IEEE/RSJ, 2012.
- [54] Edgar Sucar, Shikun Liu, Joseph Ortiz, and Andrew J. Davison. iMAP: Implicit Mapping and Positioning in Real-Time. In *International Conference on Computer Vision (ICCV)*. IEEE/CVF, 2021.
- [55] Jiaming Sun, Yiming Xie, Linghao Chen, Xiaowei Zhou, and Hujun Bao. Neuralrecon: Real-time coherent 3d reconstruction from monocular video. In *IEEE/CVF Conference*

- on *Computer Vision and Pattern Recognition*, pages 15598–15607, 2021.
- [56] Matthew Tancik, Pratul Srinivasan, Ben Mildenhall, Sara Fridovich-Keil, Nithin Raghavan, Utkarsh Singhal, Ravi Ramamoorthi, Jonathan Barron, and Ren Ng. Fourier features let networks learn high frequency functions in low dimensional domains. *Advances in Neural Information Processing Systems*, 33:7537–7547, 2020.
- [57] Yijie Tang, Jiazhao Zhang, Zhinan Yu, He Wang, and Kai Xu. Mips-fusion: Multi-implicit-submaps for scalable and robust online neural rgb-d reconstruction. *arXiv preprint arXiv:2308.08741*, 2023.
- [58] Zachary Teed and Jia Deng. Droid-slam: Deep visual slam for monocular, stereo, and rgb-d cameras. *Advances in neural information processing systems*, 34:16558–16569, 2021.
- [59] Emanuele Vespa, Nikolay Nikolov, Marius Grimm, Luigi Nardi, Paul HJ Kelly, and Stefan Leutenegger. Efficient octree-based volumetric slam supporting signed-distance and occupancy mapping. *IEEE Robotics and Automation Letters*, 3(2):1144–1151, 2018.
- [60] Hao Wang, Jun Wang, and Wang Liang. Online reconstruction of indoor scenes from rgb-d streams. In *Proceedings of the IEEE Conference on Computer Vision and Pattern Recognition*, pages 3271–3279, 2016.
- [61] Hengyi Wang, Jingwen Wang, and Lourdes Agapito. Co-slam: Joint coordinate and sparse parametric encodings for neural real-time slam. In *Proceedings of the IEEE/CVF Conference on Computer Vision and Pattern Recognition*, pages 13293–13302, 2023.
- [62] Jingwen Wang, Tymoteusz Bleja, and Lourdes Agapito. Go-surf: Neural feature grid optimization for fast, high-fidelity rgb-d surface reconstruction. In *International Conference on 3D Vision*, 2022.
- [63] Peng Wang, Lingjie Liu, Yuan Liu, Christian Theobalt, Taku Komura, and Wenping Wang. NeuS: Learning Neural Implicit Surfaces by Volume Rendering for Multi-view Reconstruction. In *Advances in Neural Information Processing Systems (NeurIPS)*, 2021.
- [64] Zhou Wang, Alan C Bovik, Hamid R Sheikh, and Eero P Simoncelli. Image quality assessment: from error visibility to structural similarity. *IEEE transactions on image processing*, 13(4):600–612, 2004.
- [65] Zirui Wang, Shangzhe Wu, Weidi Xie, Min Chen, and Victor Adrian Prisacariu. Nerf-: Neural radiance fields without known camera parameters. *arXiv preprint arXiv:2102.07064*, 2021.
- [66] Silvan Weder, Johannes Schonberger, Marc Pollefeys, and Martin R Oswald. Routedfusion: Learning real-time depth map fusion. In *IEEE/CVF Conference on Computer Vision and Pattern Recognition*, pages 4887–4897, 2020.
- [67] Silvan Weder, Johannes L Schonberger, Marc Pollefeys, and Martin R Oswald. Neurfusion: Online depth fusion in latent space. In *IEEE/CVF Conference on Computer Vision and Pattern Recognition*, pages 3162–3172, 2021.
- [68] Thibaut Weise, Thomas Wismer, Bastian Leibe, and Luc Van Gool. Online loop closure for real-time interactive 3d scanning. *Computer Vision and Image Understanding*, 115(5):635–648, 2011.
- [69] Thomas Whelan, John McDonald, Michael Kaess, Maurice Fallon, Hordur Johannsson, and John J. Leonard. Kintinuous: Spatially extended kinectfusion. In *Proceedings of RSS '12 Workshop on RGB-D: Advanced Reasoning with Depth Cameras*, 2012.
- [70] Thomas Whelan, Michael Kaess, Hordur Johannsson, Maurice Fallon, John J Leonard, and John McDonald. Real-time large-scale dense rgb-d slam with volumetric fusion. *The International Journal of Robotics Research*, 34(4-5):598–626, 2015.
- [71] Thomas Whelan, Stefan Leutenegger, Renato Salas-Moreno, Ben Glocker, and Andrew Davison. Elasticfusion: Dense slam without a pose graph. In *Robotics: Science and Systems (RSS)*, 2015.
- [72] Zhixin Yan, Mao Ye, and Liu Ren. Dense visual slam with probabilistic surfel map. *IEEE transactions on visualization and computer graphics*, 23(11):2389–2398, 2017.
- [73] Xingrui Yang, Hai Li, Hongjia Zhai, Yuhang Ming, Yuqian Liu, and Guofeng Zhang. Vox-fusion: Dense tracking and mapping with voxel-based neural implicit representation. In *IEEE International Symposium on Mixed and Augmented Reality (ISMAR)*, pages 499–507. IEEE, 2022.
- [74] Xingrui Yang, Yuhang Ming, Zhaopeng Cui, and Andrew Calway. Fd-slam: 3-d reconstruction using features and dense matching. In *2022 International Conference on Robotics and Automation (ICRA)*, pages 8040–8046. IEEE, 2022.
- [75] Richard Zhang, Phillip Isola, Alexei A Efros, Eli Shechtman, and Oliver Wang. The unreasonable effectiveness of deep features as a perceptual metric. In *IEEE conference on computer vision and pattern recognition*, pages 586–595, 2018.
- [76] Youmin Zhang, Fabio Tosi, Stefano Mattocchia, and Matteo Poggi. Go-slam: Global optimization for consistent 3d instant reconstruction. *arXiv preprint arXiv:2309.02436*, 2023.
- [77] Zihan Zhu, Songyou Peng, Viktor Larsson, Weiwei Xu, Hujun Bao, Zhaopeng Cui, Martin R Oswald, and Marc Pollefeys. Nice-slam: Neural implicit scalable encoding for slam. In *IEEE/CVF Conference on Computer Vision and Pattern Recognition*, pages 12786–12796, 2022.
- [78] Zihan Zhu, Songyou Peng, Viktor Larsson, Zhaopeng Cui, Martin R Oswald, Andreas Geiger, and Marc Pollefeys. Nicer-slam: Neural implicit scene encoding for rgb slam. *arXiv preprint arXiv:2302.03594*, 2023.

# Loopy-SLAM: Dense Neural SLAM with Loop Closures

## Supplementary Material

### Abstract

This supplementary material accompanies the main paper by providing further information for better reproducibility as well as additional evaluations and qualitative results.

### A. Video

We provide a video along with the supplementary material showing the online reconstruction process with loop closure on scene 54 from the ScanNet [12] dataset. We show the ground truth trajectory in black and the estimated in red. Furthermore, we display each submap individually to show the map deformations. When loop closure is triggered, the global trajectory along with the associated submaps are rigidly corrected. Note in particular the important loop closure that is triggered when the camera moves into the hallway of the scene. At the end of the trajectory, we show the final globally fused mesh (different from the union of the submap meshes we show during runtime).

### B. Implementation Details

On Replica [51] and ScanNet [12], we enforce the restriction that a loop closure edge cannot be a direct neighbor between two submaps (then they relate to each other by an odometry edge) *i.e.* the distance between two submaps needs to be at least two. On TUM-RGBD [53] we instead only accept a loop edge if the distance between the two submaps is at least three. We use PyTorch 1.12 and Python 3.10 to implement the pipeline. Training is done with the Adam optimizer and the default hyperparameters  $\text{betas} = (0.9, 0.999)$ ,  $\text{eps} = 1e-08$  and  $\text{weight\_decay} = 0$ . The results are gathered using various Nvidia GPUs, all with a maximum memory of 12 GB. Tab. 7 describes other dataset-specific hyperparameters such as the mapping window size which describes how many frames (current frame and selected keyframes) are used during mapping. We also follow [77] and use a simple keyframe selection strategy which adds frames to the keyframe database at regular intervals (see also Tab. 7). Regarding optimization specific hyperparameters like learning rate, we adopt the values found by [45].

### C. Evaluation Metrics

**Mapping.** We use the following five metrics to quantify the reconstruction performance. We compare the ground

Dataset	Map Every	Keyframe Every	Map Window	Track Iter.	Map Iter.
Replica [51]	5	5	12	40	300
TUM-RGBD [53]	2	10	10	200	150
ScanNet [12]	5	10	20	100	300

Table 7. **Parameter Configurations on Tested Datasets.** Map Every: how often (in frames) mapping is done. Keyframe Every: How often *local* keyframes are added. Note that these are deleted when the next submap is initialized and are not kept in memory. Map Window: How many keyframes that are sampled to overlap with the current viewing frustum for mapping. Iter.: Iterations (optimization steps).

truth mesh to the predicted mesh. The F-score is defined as the harmonic mean between Precision (P) and Recall (R),  $F = 2 \frac{PR}{P+R}$ . Precision is defined as the percentage of points on the predicted mesh which lie within some distance  $\tau$  from a point on the ground truth mesh. Vice versa, Recall is defined as the percentage of points on the ground truth mesh which lie within the same distance  $\tau$  from a point on the predicted mesh. In all our experiments, we use a distance threshold  $\tau = 0.01$  m. Before the Precision and Recall are computed, the input meshes are aligned with the iterative closest point (ICP) algorithm. We use the evaluation script provided by the authors of [44] \*. Finally, we report the depth L1 metric which renders depth maps from randomly sampled view points from the reconstructed and ground truth meshes. The depth maps are then compared and the L1 error is reported and averaged over 1000 sampled views. We use the evaluation code provided by [77].

**Tracking.** We use the absolute trajectory error (ATE) RMSE [53] to compare tracking error across methods. This computes the translation difference between the estimated trajectory and the ground truth. Before evaluating the ATE RMSE, we align the trajectories with Horn’s closed form solution [19].

### D. Comment on Bundle Adjustment

In this work, we do not study the effect of performing Bundle Adjustment (BA), which may be used as a refinement step besides mapping, tracking and loop closure. To reduce intra-submap drift, local BA may potentially be applied in an online fashion and/or global BA could be applied at the end of trajectory capture. This topic deserves a thorough experimental evaluation which we leave for future work.

\*[https://github.com/eriksandroem/evaluate\\_3d\\_reconstruction\\_lib](https://github.com/eriksandroem/evaluate_3d_reconstruction_lib)

Method	00	59	106	169	181	207	54	233	465	Avg.
# Frames	5578	1807	2324	2034	2349	1988	6629	7643	6306	4073
PGOs	47	14	8	13	29	9	51	37	33	27

Table 8. **Number of PGOs on ScanNet [12]**. On average, loop closure is triggered every 151 frames.

Max iter.	Conf. thresh.	sec/reg.	ATE [cm]
10M	0.99999	29.85	7.61
100K	0.95	6.88	8.94
50K	0.95	6.52	7.96

Table 9. **Ablation on Global Registration Settings**. We show the average time per global registration for different settings of the stopping criteria *i.e.* max iterations and the confidence threshold. The runtime can be improved when we are more conservative with the stopping criteria without affecting the ATE RMSE to a significant extent. The numbers are from a single run on the `fr1 room` scene.

## E. Additional Experiments

**Number of PGOs per Frame.** Tab. 8 shows the number of pose graph optimizations (PGOs) per scene that is performed. On average, loop closure is triggered once every 151 frames.

**Ablation on Global Registration Settings.** Tab. 9 shows the average time per registration and the final ATE RMSE for different settings of the global registration strategy. Specifically, we vary the stopping criteria. Global registration is stopped if the maximum specified iterations or the confidence threshold for the registration is reached. We show the results for a single run on the TUM-RGBD [53] `fr1 room` scene. For the results in the main paper, the maximum iterations is set to 10M and the confidence threshold to 0.99999. We find that these settings can be relaxed greatly, with benefits to the registration speed. We report the numbers on an AMD EPYC 7742 processor. The runtime of 12 sec/reg. in the main paper was reported on an 11th Gen Intel® Core™ i7-11800H processor.

**Odometry Tracking Accuracy.** Tab. 10 shows the tracking accuracy when deactivating loop closure and running our system similar to Point-SLAM [45], but with submap creation. Creating submaps without loop closure leads unavoidably to some more camera drift compared to standard Point-SLAM, since the frame-to-model tracker becomes less robust. The degradation is, however, not very strong.

**Qualitative Renderings.** In Fig. 5 and Fig. 6 we show renderings from the Replica [51] and TUM-RGBD [53] datasets respectively. Our method is compared to ES-LAM [28] and Point-SLAM [45]. Unfortunately, rendering using GO-SLAM [76] was not working at the time of submission.

**Precision and Recall Reconstruction Metrics.** In Tab. 11

Method	LC	of0	of1	of2	of3	of4	rm0	rm1	rm2	Avg.
Point-SLAM [45]	✗	0.61	0.41	0.37	0.38	0.48	0.54	0.69	0.72	0.52
Ours	✗	0.63	0.58	0.72	0.75	1.28	0.61	0.44	0.53	0.69
<b>Ours</b>	✓	<b>0.24</b>	<b>0.24</b>	<b>0.28</b>	<b>0.26</b>	<b>0.40</b>	<b>0.29</b>	<b>0.22</b>	<b>0.35</b>	<b>0.29</b>

Table 10. **Odometry Performance on Replica [51]**. The performance when removing loop closure, but keeping the submap creation of our method, does not lead to a substantial drop in tracking accuracy compared to Point-SLAM. LC denotes if loop closure is enabled or disabled.

we additionally show Precision and Recall compared to the main paper per scene on the Replica [51] dataset.

**Qualitative Mesh Visualizations.** In Figs. 7 to 9 we show additional mesh visualizations on the Replica [51] dataset. We show the textured meshes as well as the meshes with normal shading.

**Importance of Feature Refinement.** In Fig. 10 we show renderings before and after feature refinement from `office 1` on the Replica [51] dataset. Since the color decoder is optimized on the fly, it is typically not suitable to render from all poses at the end of trajectory capture (the problem is sometimes referred to as the forgetting problem). Regardless, as both the color and geometric features are globally refined, the feature refinement step is useful because it weakens the assumption of small intra-submap drift. By optimizing the color and geometric features, we guarantee consistent transitions in texture and geometry between submaps. Note specifically that the refinement from one of the last poses (1995) is much smaller compared to the first frame. This demonstrates the forgetting problem. We experimented with a fixed color decoder, but found that this negatively impacted tracking somewhat. We leave it as future work to learn a robust color decoder.

**Rendering with and without Feature Fusion.** In Fig. 11 we show renderings after feature refinement when enabling and disabling feature fusion. The primary reason for doing feature fusion is to remove redundancies between submaps which saves memory and speeds up the refinement step. Nonetheless, we observe a small improvement in rendering quality from doing this as a bonus.

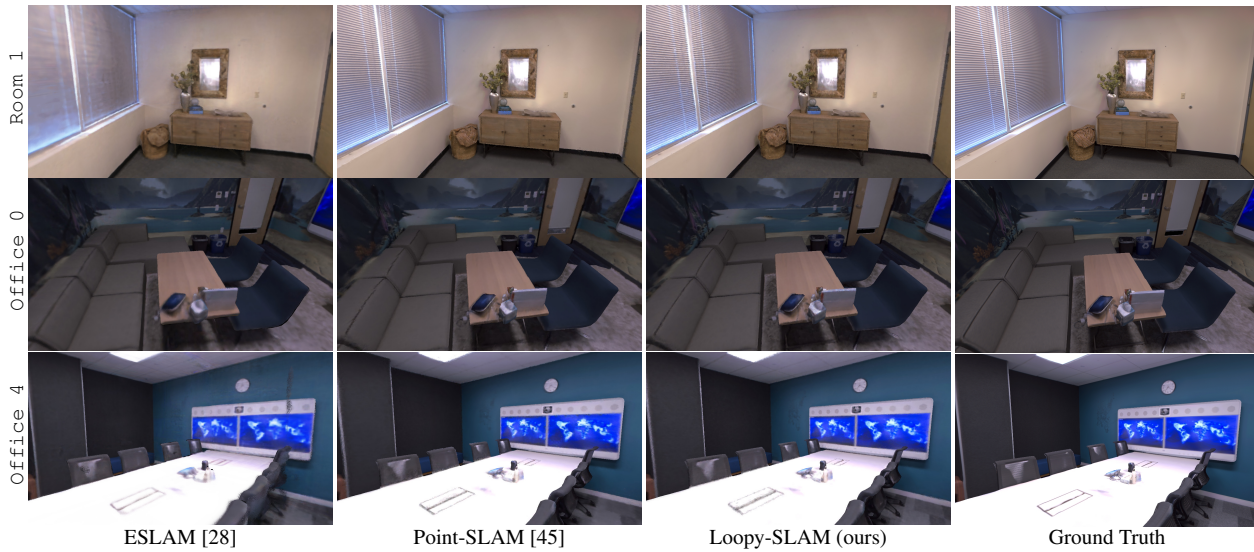


Figure 5. **Rendering Performance on Replica [51]**. The rendering performance is comparable to Point-SLAM [45], which is expected given that the same neural point cloud scene representation is used.

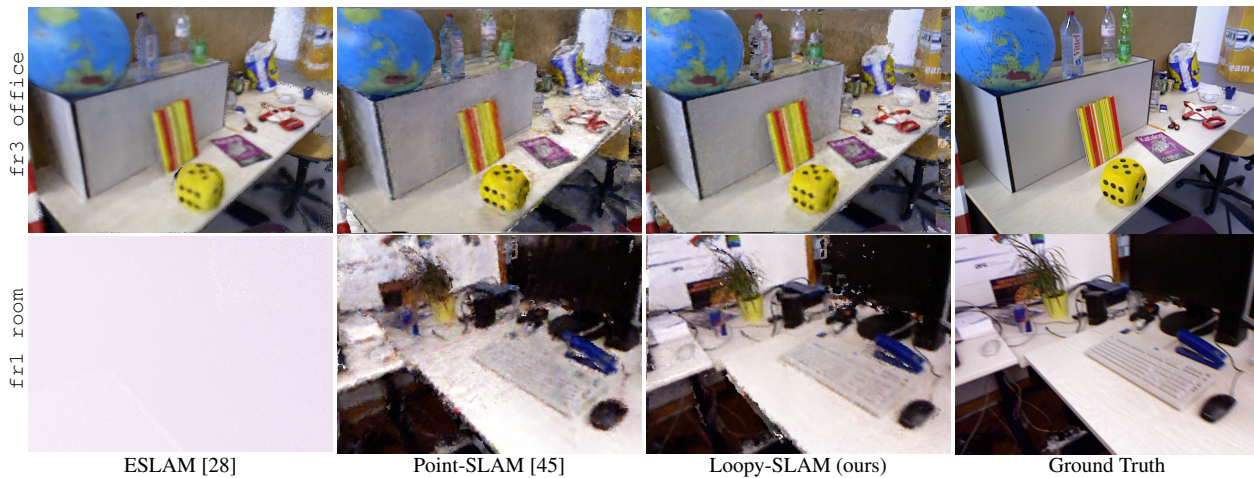


Figure 6. **Rendering Performance on TUM-RGBD [53]**. The rendering performance is comparable to Point-SLAM [45], which is expected given that the same neural point cloud scene representation is used. In some cases, due to camera pose drift in Point-SLAM, our method yields better renderings. We note that ESLAM loses tracking severely on the `fr1_room` scene which results in failed renderings.

Method	Metric	Rm 0	Rm 1	Rm 2	Off 0	Off 1	Off 2	Off 3	Off 4	Avg.
NICE-SLAM [77]	Depth L1 [cm] ↓	1.81	1.44	2.04	1.39	1.76	8.33	4.99	2.01	2.97
	Precision [%] ↑	45.86	43.76	44.38	51.40	50.80	38.37	40.85	37.35	44.10
	Recall [%] ↑	44.10	46.12	42.78	48.66	53.08	39.98	39.04	35.77	43.69
	F1 [%] ↑	44.96	44.84	43.56	49.99	51.91	39.16	39.92	36.54	43.86
Vox-Fusion [73]	Depth L1 [cm] ↓	1.09	1.90	2.21	2.32	3.40	4.19	2.96	1.61	2.46
	Precision [%] ↑	75.83	35.88	63.10	48.51	43.50	54.48	69.11	55.40	55.73
	Recall [%] ↑	64.89	33.07	56.62	44.76	38.44	47.85	60.61	46.79	49.13
	F1 [%] ↑	69.93	34.38	59.67	46.54	40.81	50.95	64.56	50.72	52.20
ESLAM [28]	Depth L1 [cm] ↓	0.97	1.07	1.28	0.86	1.26	1.71	1.43	1.06	1.18
	Precision [%] ↑	75.25	77.72	82.59	70.73	67.5	71.81	72.1	76.28	74.25
	Recall [%] ↑	87.59	87.24	85.33	87.81	85.62	83.34	79.15	82.23	84.79
	F1 [%] ↑	80.96	82.21	83.94	78.36	75.49	77.14	75.46	79.14	79.09
Co-SLAM [61]	Depth L1 [cm] ↓	1.05	0.85	2.37	1.24	1.48	1.86	1.66	1.54	1.51
GO-SLAM [76]	Depth L1 [cm] ↓	-	-	-	-	-	-	-	-	3.38
	*Depth L1 [cm] ↓	4.56	1.97	3.43	2.47	3.03	10.3	7.31	4.34	4.68
	Precision [%] ↑	20.15	38.23	28.45	49.48	37.18	25.45	20.45	26.45	30.73
	Recall [%] ↑	15.21	29.54	20.82	37.97	27.78	19.13	15.03	18.85	23.04
	F1 [%] ↑	17.34	33.4	24.04	43.0	31.8	21.84	17.32	22.01	26.34
Point-SLAM [45]	Depth L1 [cm] ↓	0.53	0.22	0.46	0.30	0.57	<b>0.49</b>	0.51	0.46	0.44
	Precision [%] ↑	91.95	99.04	<b>97.89</b>	99.00	99.37	<b>98.05</b>	96.61	93.98	96.99
	Recall [%] ↑	82.48	86.43	<b>84.64</b>	89.06	<b>84.99</b>	<b>81.44</b>	81.17	78.51	83.59
	F1 [%] ↑	86.90	92.31	<b>90.78</b>	93.77	<b>91.62</b>	<b>88.98</b>	88.22	85.55	89.77
<b>Ours</b>	Depth L1 [cm] ↓	<b>0.30</b>	<b>0.20</b>	<b>0.42</b>	<b>0.23</b>	<b>0.46</b>	0.60	<b>0.37</b>	<b>0.24</b>	<b>0.35</b>
	Precision [%] ↑	<b>98.85</b>	<b>99.21</b>	97.84	<b>99.18</b>	<b>99.44</b>	97.78	<b>98.10</b>	<b>97.86</b>	<b>98.53</b>
	Recall [%] ↑	<b>85.29</b>	<b>86.44</b>	84.38	<b>89.12</b>	84.88	80.89	<b>81.36</b>	<b>81.07</b>	<b>84.18</b>
	F1 [%] ↑	<b>91.57</b>	<b>92.39</b>	90.61	<b>93.88</b>	91.58	88.54	<b>88.95</b>	<b>88.68</b>	<b>90.77</b>

Table 11. **Reconstruction Performance on Replica [51]**. Our method performs better than all existing methods on average. \*Depth L1 for GO-SLAM shows our reproduced results from random poses (GO-SLAM evaluates on ground truth poses).

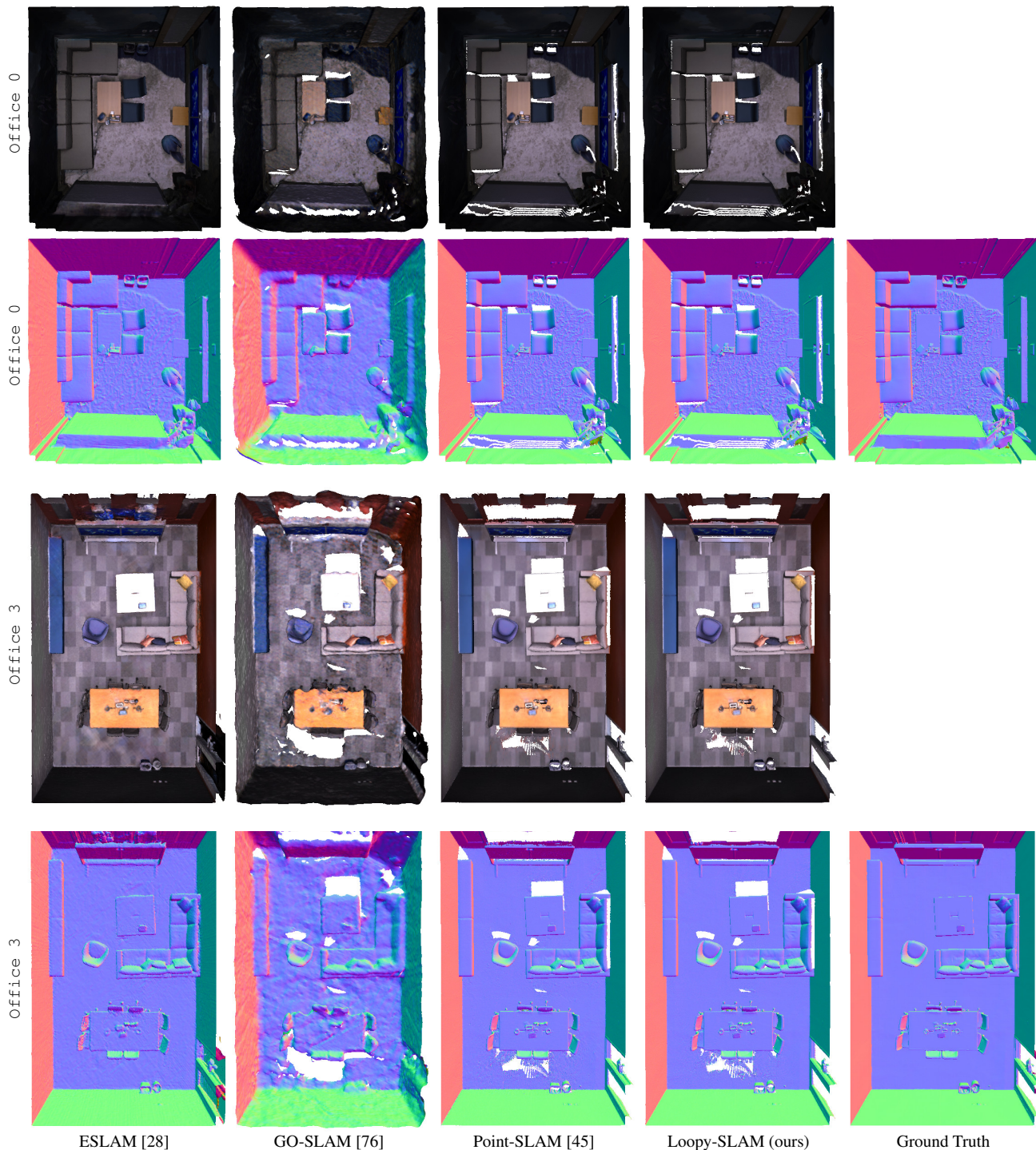


Figure 7. **Rendering Performance on Replica [51]**. The rendering performance is comparable to Point-SLAM [45], which is expected given that the same neural point cloud scene representation is used. Note that ground truth mesh with accurate texture are not publicly available.



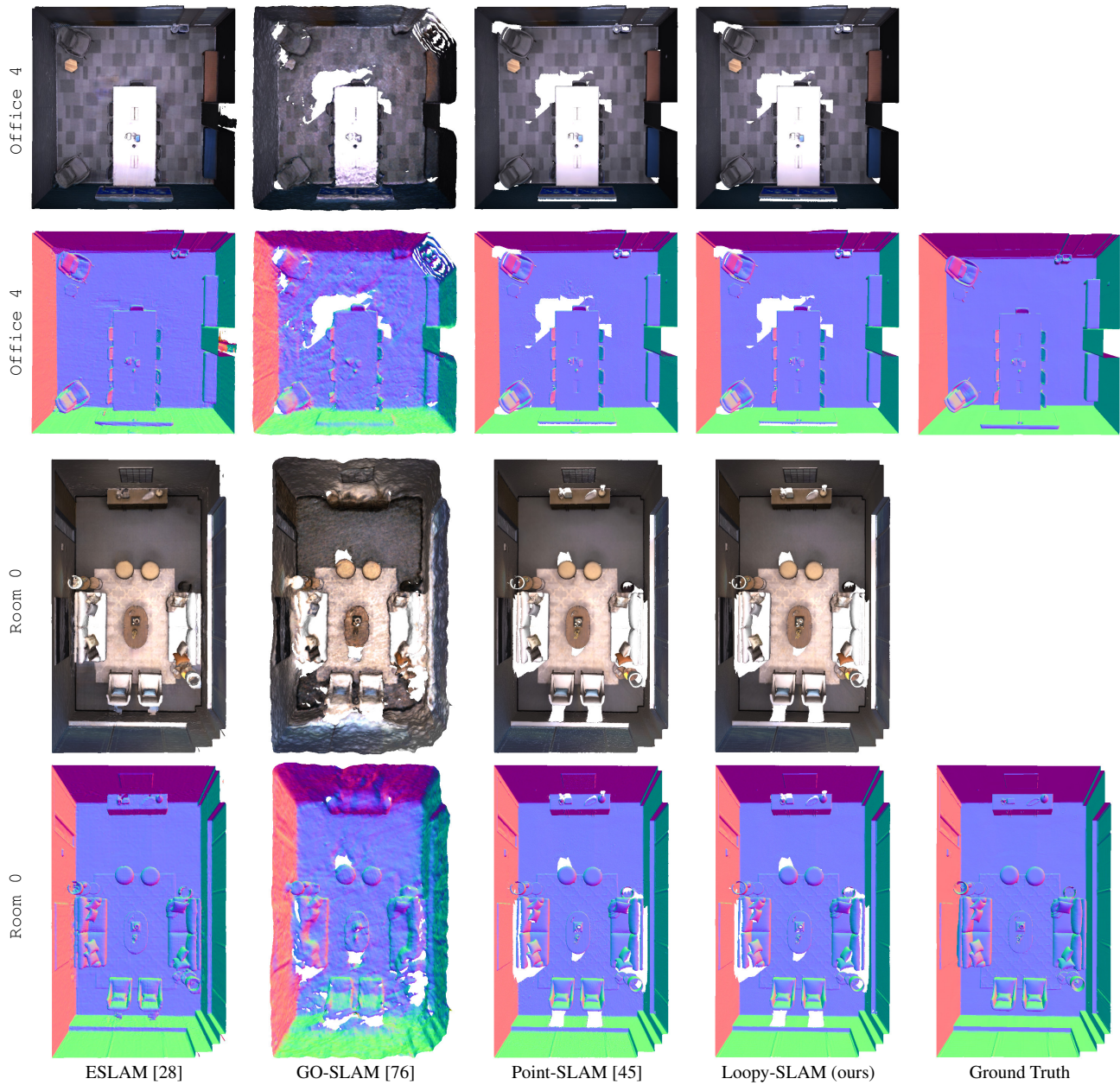


Figure 8. **Rendering Performance on Replica [51]**. The rendering performance is comparable to Point-SLAM [45], which is expected given that the same neural point cloud scene representation is used. Note that ground truth mesh with accurate texture are not publicly available.

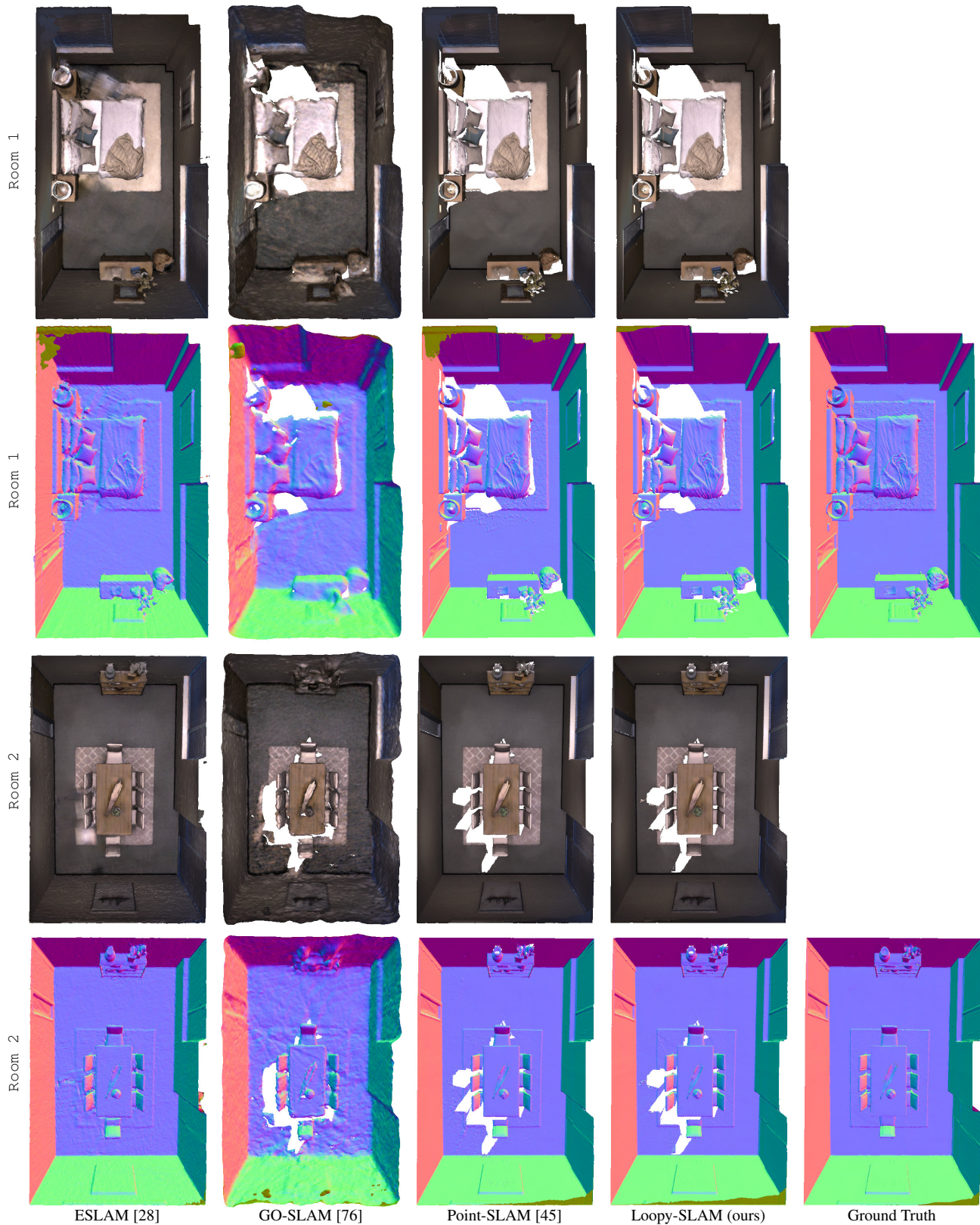


Figure 9. **Rendering Performance on Replica [51]**. The rendering performance is comparable to Point-SLAM [45], which is expected given that the same neural point cloud scene representation is used. Note that ground truth mesh with accurate texture are not publicly available.

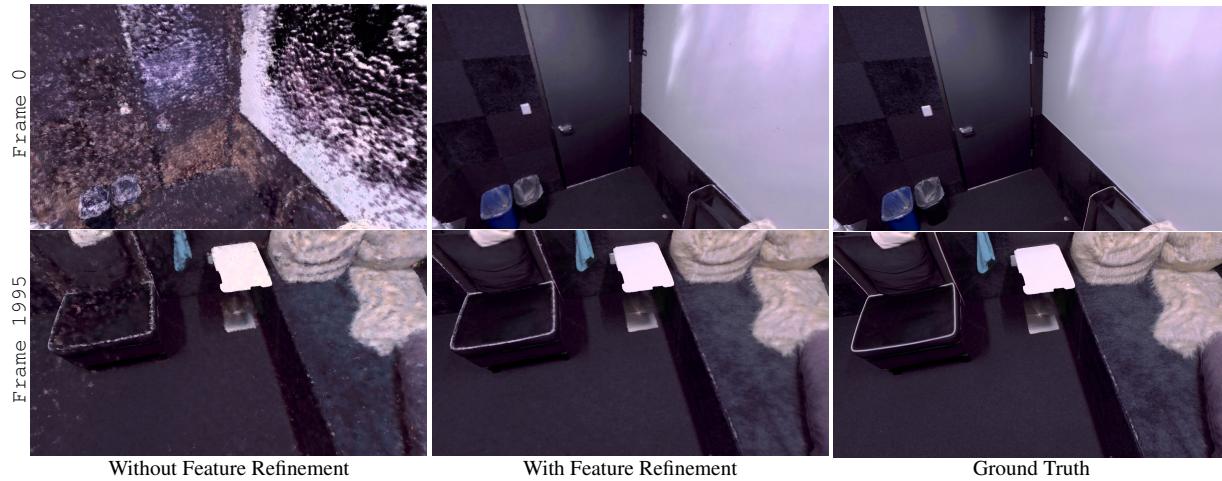


Figure 10. **Importance of Feature Refinement.** We show renderings before and after feature refinement from `office 1` on the Replica [51] dataset. Since the color decoder is optimized on the fly, it is typically not suitable to render from all poses at the end of trajectory capture (the problem is sometimes referred to as the forgetting problem). To demonstrate the forgetting problem, we render from the first pose and one of the last poses. The refinement from pose zero is much greater compared to pose 1995. We experimented with a fixed color decoder, but found that this negatively impacted tracking somewhat. We leave it as future work to learn a robust color decoder.

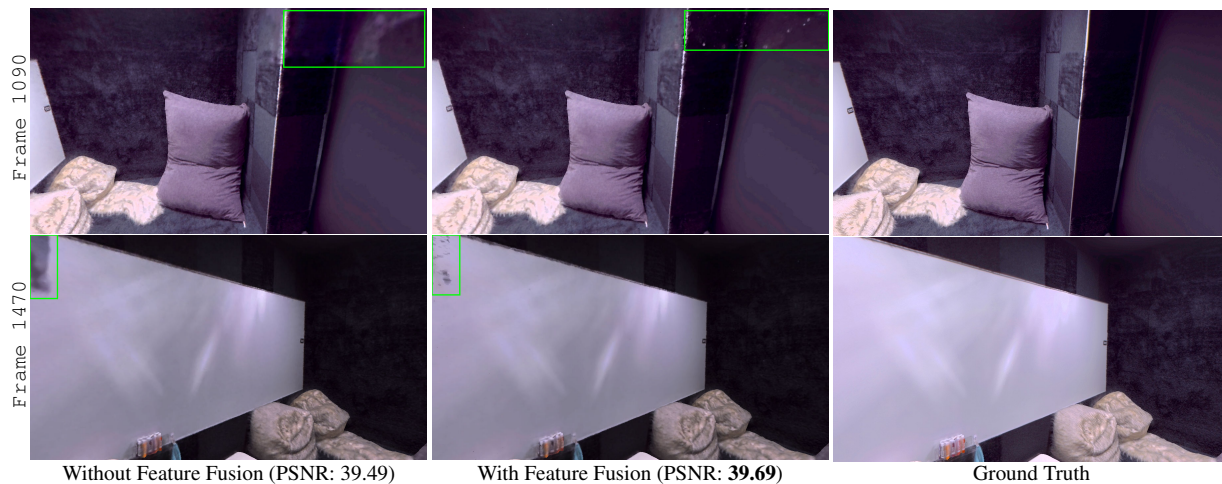


Figure 11. **Importance of Feature Refinement.** We show renderings with and without feature fusion (after feature refinement) from `office 1` on the Replica [51] dataset. We note small improvements in rendering quality when using feature fusion (see green boxes).